

**Evaluation of dosimetry, quantitative methods and test-retest variability of  $^{18}\text{F}$ -PI-2620 PET for the assessment of tau deposits in the human brain**

**Authors**

Santiago Bullich<sup>1</sup>, Olivier Barret<sup>2</sup>, Cristian Constantinescu<sup>2</sup>, Christine Sandiego<sup>2</sup>, Andre Mueller<sup>1</sup>, Mathias Berndt<sup>1</sup>, Caroline Papin<sup>1,2</sup>, Audrey Perrotin<sup>1</sup>, Norman Koglin<sup>1</sup>, Heiko Kroth<sup>3</sup>, Andrea Pfeifer<sup>3</sup>, Gilles Tamagnan<sup>2</sup>, Jennifer Madonia<sup>2</sup>, John P. Seibyl<sup>2</sup>, Kenneth Marek<sup>2</sup>, Susan de Santi<sup>4</sup>, Ludger M. Dinkelborg<sup>1</sup>, Andrew W. Stephens<sup>1</sup>

<sup>1</sup> *Life Molecular Imaging GmbH, Berlin, Germany*

<sup>2</sup> *Invicro, New Haven, Connecticut, USA*

<sup>3</sup> *AC Immune SA, Lausanne, Switzerland*

<sup>4</sup> *Life Molecular Imaging Inc, Boston, MA, USA*

**Corresponding Author:**

Andrew W. Stephens, MD, PhD  
Life Molecular Imaging GmbH  
Tegeler Straße 6-7, 13353 Berlin, Germany  
Email: [a.stephens@life-mi.com](mailto:a.stephens@life-mi.com)  
Phone: +49-30461124603  
Fax: +49-30461124629

**First Author:**

Santiago Bullich, PhD  
Life Molecular Imaging GmbH  
Tegeler Straße 6-7, 13353 Berlin, Germany  
Email: [s.bullich@life-mi.com](mailto:s.bullich@life-mi.com)  
Phone: +49-30461124603  
Fax: +49-30461124629

Word count of the manuscript: 5137

Financial support: Life Molecular Imaging

Short running title:  $^{18}\text{F}$ -PI-2620 kinetics and quantification

## Abstract

<sup>18</sup>F-PI-2620 is a next generation tau positron emission tomography (PET)-tracer that has demonstrated ability to image the spatial distribution of suspected tau pathology. The objective of this study was to assess the tracer biodistribution, dosimetry and quantitative methods of <sup>18</sup>F-PI-2620 in the human brain. Full kinetic modelling approaches to quantify tau load were investigated. Non-invasive kinetic modeling approaches and semi-quantitative methods were evaluated against the full tracer kinetics. Finally, the reproducibility of PET measurements from test and retest scans was assessed. **Methods.** Three healthy controls (HC) and 4 Alzheimer disease (AD) subjects underwent two dynamic PET scans including arterial sampling. Distribution volume ratio (DVR) was estimated using full tracer kinetics (2 Tissue Compartment (2TC) models, Logan Graphical Analysis (LGA)) and non-invasive kinetic models (Non-Invasive Logan Graphical Analysis (NI-LGA) and the multilinear reference tissue model (MRTM2)). Standardized uptake value ratio (SUVR) was determined at different imaging windows after injection. Correlation between DVR and SUVR, effect size (Cohen's d) and test-retest variability (TRV) were evaluated. Additionally, 6 HC subjects received one tracer administration and underwent whole-body PET for dosimetry calculation. Organ doses and the whole-body effective dose were calculated using OLINDA 2.0. **Results.** Strong correlation was found across different kinetic models ( $R^2 > 0.97$ ) and between DVR(2TC) and SUVRs between 30 to 90 min with  $R^2 > 0.95$ . Secular equilibrium was reached around 40 min post injection (p.i.) in most regions and subjects. The TRV and effect size for the SUVR across different regions was similar at 30-60 min (TRV=3.8%, d=3.80), 45-75 min (TRV=4.3%, d=3.77) and 60-90 min (TRV=4.9%, d=3.73) and increased at later time points. Elimination was via the hepatobiliary and urinary system. The whole-body effective dose was determined to be  $33.3 \pm 2.1$   $\mu$ Sv/MBq for an adult female and  $33.1 \pm 1.4$   $\mu$ Sv/MBq for an adult male with a 1.5 hour urinary bladder voiding interval. **Conclusion.** <sup>18</sup>F-PI-2620 exhibits fast kinetics, suitable dosimetry and low TRV. DVR measured using the 2TC model with arterial sampling correlated strongly with DVR measured by NI-LGA, MRTM2 and SUVR. SUVR can be used for <sup>18</sup>F-PI-2620 PET quantification of tau deposits avoiding arterial blood sampling. Static <sup>18</sup>F-PI-2620 PET scans between 45-75min p.i. provide excellent quantification accuracy, large effect size and low TRV.

**Key words:** tau PET; PI-2620; Alzheimer's disease; test-retest; dosimetry

## INTRODUCTION

Alzheimer's disease (AD) is the most common cause of dementia among elderly adults, which is characterized by memory loss, spatial disorientation and cognitive impairment. Key pathologic features of AD include extracellular amyloid- $\beta$  ( $A\beta$ ) aggregates and intracellular tau neurofibrillary tangles (1). In particular, the role of tau phosphorylation in the pathophysiology of tauopathies remains only partially understood. As consequence, accurate quantification of tau neurofibrillary tangles in the living brain is critical to expand current knowledge of the role of tau in tauopathies (1). Several positron emission tomography (PET) tracers targeting tau have been discovered and are currently being tested in humans (2,3).

$^{18}\text{F}$ -PI-2620 is a next generation tau PET tracer with high binding affinity for aggregated tau of both, 3R and 4R isoforms, without specific tracer binding on brain slices from non-demented donors (4). This compound showed high selectivity with no off-target binding to beta-amyloid or monoamine oxidase A/B, and high initial brain uptake and fast wash-out was observed in animal models (4). Initial clinical investigations confirmed the preclinical data and showed that  $^{18}\text{F}$ -PI-2620 is safe and accumulates in regions known to have tau deposition in AD subjects (5). Healthy controls (HC) showed very low  $^{18}\text{F}$ -PI-2620 accumulation, and AD subjects could be clearly distinguished from HC (5). Although visual assessment has shown to be suitable for detection of tau deposits in AD, it may not sufficiently describe subtle longitudinal changes or tau deposition in early stages of the disease. Consequently, reliable quantitation of the tau load in the brain is critical in the research setting either in observational clinical studies or interventional therapeutic trials.

The objectives of this study were: (i) to describe the biodistribution and dosimetry of  $^{18}\text{F}$ -PI-2620, (ii) to assess the tracer kinetics of  $^{18}\text{F}$ -PI-2620 in the human brain, (iii) to identify optimal full kinetic modelling approaches to quantify tau load in the human brain using  $^{18}\text{F}$ -PI-2620, (iv) to assess the validity of non-invasive kinetic modeling approaches and semi-quantitative methods, and (v) to assess the reproducibility of PET measurements with test-retest scans.

## MATERIALS AND METHODS

### Subjects

The study population consisted of 9 HC and 4 AD subjects. Three male and three female HC (age range: 19-47 years) underwent a whole-body PET scan to assess biodistribution and dosimetry of  $^{18}\text{F}$ -PI-

2620. Three elderly HC (age range: 61-75 years) and 4 AD subjects (age range: 58-71 years) underwent one  $^{18}\text{F}$ -florbetaben and two  $^{18}\text{F}$ -PI-2620 brain PET scans with arterial blood sampling. A T1-weighted magnetic resonance imaging (MRI) scan was acquired for each subject on a Siemens Espree 1.5 Tesla to confirm eligibility criteria and to identify and delineate brain anatomical regions of interest (ROI). This study was conducted in accordance with the Declaration of Helsinki. The study protocol was reviewed and approved by the New England Institutional Review Board. All participants (or their legal representatives) provided written informed consent and underwent screening evaluation including baseline clinical laboratory testing, a physical and neurological evaluation and cognitive assessment.

### **Radiotracer Preparation**

$^{18}\text{F}$ -PI-2620 was synthesized using a GE TRACERlab FX-FN as recently described (4).  $^{18}\text{F}$ -PI-2620 was obtained with  $16.2\pm 4.9\%$  radiochemical yield (decay corrected),  $99.6\pm 1.6\%$  radiochemical purity and molar activity of  $188.3\pm 66.6$  GBq  $\mu\text{mol}^{-1}$ . Neuraceq (florbetaben  $^{18}\text{F}$ ) was obtained from SOFIE (Totowa, NJ).

### **Biodistribution and Dosimetry Study**

*Whole Body Acquisition.* Immediately following intravenous bolus administration of  $^{18}\text{F}$ -PI-2620, a series of whole-body PET images consisting of 9 bed positions was acquired from the vertex of the head to the thighs over a period of 5.5 hours in three scanning sessions using a Siemens Biograph PET/CT camera. The scanning sessions were separated by 30 min breaks during which the subjects were allowed to leave the scanner bed. The first scanning session included 5 whole body passes ( $2\times 60$ , and  $3\times 120$  seconds per bed position). The second and third session included 2 whole body passes each ( $2\times 270$  seconds per bed position). A whole-body CT transmission scan was acquired prior to each imaging session. Urine collection was performed 3-4 times, 1-2 times after each scanning session, up to 6 hours post radiotracer injection to measure the excretion of  $^{18}\text{F}$ -PI-2620 through the urinary tract.

*Dosimetry Estimation.* Manually delineated ROI were placed on the visually identified source organs (brain, lungs, heart wall, liver, gallbladder, intestines, marrow, kidneys, and urinary bladder), which were subsequently used for all the study PET frames. Each ROI covered the whole organ, with the exception of bone marrow ROI which only included the lumbar spine. Radioactivity was corrected for body attenuation, but not for decay, and time activity curves (TACs) generated for each source organ. Source organs TACs were then expressed as percent injected dose by normalization to the injected activity. Organ residence times were computed from area under the non-decay corrected TACs via trapezoid

method. Area under the curve from end of imaging to infinity was computed with the assumption of physical decay only following the last imaging time point. The residence time for all the source organs were summed and subtracted from the theoretical total residence time value to calculate the residence time of the remainder of the body. The ICRP30 gastrointestinal tract model was applied in order to compute residence times in the small intestine, lower and upper large intestine, with the assumption that activity enters the gastrointestinal tract via the small intestine, where the intestinal decay corrected time-activity curve was used for estimation of the fraction of the radioactivity entering the intestine during the imaging period. A gallbladder emptying model was employed and gallbladder residence times were computed based on the model assumptions. Calculations were performed with and without modeling of urinary bladder voiding. When urinary bladder excretion was modeled, the residence times were calculated by fitting an exponential to the combined cumulative urinary bladder imaging data with the measured urine samples collected after each of the 3 scanning sessions. Parameters representing the fraction leaving the body via urine and biological half-time were obtained from the fit and used for modeling urinary bladder voiding for all subjects. Urinary bladder voiding models with voiding intervals of 1.5 hours were applied. Organ Level Internal Dose Assessment (OLINDA) EXM1.1 software package was used to estimate the organ and whole-body radiation absorbed doses (6). The 70 kg adult male and the 55 kg adult female models were used. Organ absorbed doses, effective doses, and effective dose equivalents were calculated as mean  $\pm$  standard deviation across subjects.

### **Tracer Kinetics Study**

*Image Acquisition and Reconstruction.* All subjects underwent a  $^{18}\text{F}$ -florbetaben PET according to the standard methods for screening. All eligible subjects underwent two dynamic  $^{18}\text{F}$ -PI-2620 PET scans for test-retest assessment within three weeks using a Siemens ECAT EXACT HR+ camera. Prior to the radiotracer injection and emission imaging, a transmission scan was performed with an external  $^{68}\text{Ge}$  rod source to provide correction coefficients for attenuation correction. Subjects were administered a single dose of  $^{18}\text{F}$ -PI-2620 per imaging visit ( $339.4 \pm 5.2$  MBq,  $1.4 \pm 0.7$   $\mu\text{g}$  (test) and  $339.7 \pm 7.5$  MBq,  $2.1 \pm 1.1$   $\mu\text{g}$  (retest)) as a 3-minute bolus through a venous catheter followed by a 10 mL saline flush. Dynamic PET imaging of the brain was acquired over two imaging sessions over the course of 180 min following tracer injection (0-90 min: 6x30 sec, 4x1 min, 4x2 min, 15x5 min; 120-180 min: 12x5 min). PET images were reconstructed in a 128 x 128 matrix (zoom=2, pixel size of 2.574 x 2.574 mm) with the ordered subsets expectation maximization algorithm (4 iterations, 16 subsets) and a post hoc Gaussian filter = 5 mm. Corrections for random coincidences, scatter, system dead time and attenuation were performed as provided by the camera manufacturer.

*Arterial Blood Sampling.* During  $^{18}\text{F}$ -PI-2620 PET imaging, arterial blood samples were collected at 0.75, 1.5, 2.25, 3, 3.75, 4.5, 5.25, 6, 8, 10, 15, 20, 25, 30, 45, 60, 75 and 90-min p.i.. Samples were counted to measure activity in the total plasma and whole blood samples over time. Samples at 4.5, 8, 15, 30, 60 and 90-min p.i. were analyzed to determine the unmetabolized parent fraction of  $^{18}\text{F}$ -PI-2620. Metabolite analysis and plasma protein binding (free fraction) was performed as recently described (7). The plasma activity corrected for metabolites was used as input function for tracer kinetic modeling.

*Image Analysis.* Reconstructed PET images were processed using SPM12 software (<http://www.fil.ion.ucl.ac.uk/spm/doc/>) including motion correction and co-registration onto the individual MRI. The MRI was segmented into grey matter, white matter and cerebrospinal fluid. Subsequently, MRI was normalized into the standard MNI (Montreal Neurological Institute) space and the same transformation was applied to the co-registered PET images and gray matter probability maps. ROIs were defined as the intersection between the standard Automated Anatomic Labeling (AAL) template (8) and the normalized gray matter segmentation thresholded at a probability level of 0.2. Cortical ROIs extracted from the AAL anatomical template were the amygdala, hippocampus, parahippocampus, fusiform gyrus, inferior lateral temporal, superior lateral temporal, orbitofrontal, prefrontal, occipital, parietal, anterior cingulate, posterior cingulate cortices and cerebellar gray matter. Cerebellar gray matter (CGM) excluding vermis and anterior lobe surrounding the vermis was used as reference region. Average activity concentration (kBq/mL) at each time point was determined for each ROI and TACs were generated.

*Tracer Kinetic Modelling.* TACs, plasma arterial samples corrected for metabolites and whole blood arterial samples collected up to 90 min after tracer injection were analyzed using PMOD 3.7 software package (PMOD Technologies, Zurich, Switzerland). Invasive models (1-tissue compartment (1TC) model, 2-tissue compartment (2TC) model and Logan graphical analysis (LGA,  $t^*=20$  min) were used to estimate volume of distribution ( $V_T$ ) across regions (9,10). The distribution volume ratio (DVR) using the cerebellar cortex as a reference region (RR) was computed as  $V_T/V_T(\text{RR})$  being  $V_T$  the total volume of distribution in the target ROI and  $V_T(\text{RR})$  the total volume of distribution in the reference region (9). The binding potential ( $\text{BP}_{\text{ND}}$ ) was computed as  $\text{BP}_{\text{ND}}=\text{DVR}-1$ . The DVR, using the CGM as a reference region, was also estimated using the non-invasive Logan graphical plot (NI-LGA)( $t^*=20$  min,  $k_2'=0.22$   $\text{min}^{-1}$ ) (10) and the multilinear reference tissue model (MRTM2) ( $t^*=20$  min,  $k_2'=0.22$   $\text{min}^{-1}$ ) (11). The  $k_2'$  used in the NI-LGA and MRTM2 was average  $k_2'$  derived from the full tracer kinetic modeling using a 2TC. Akaike information criterion (AIC) was used to determine the optimal kinetic modelling approach.

*Standardized Uptake Value Ratio (SUVR).* Mean radioactivity concentration (kBq/mL) at each time point was obtained from each ROI. SUVR at different time points was calculated as the ratio of the activity in the target ROI to the activity in the reference region ROI (CGM). SUVR was determined at six 30-minutes imaging windows by averaging the SUVR at different time points within each imaging window (20-50, 30-60, 45-75, 60-90, 120-150, and 150-180 min p.i.). The secular equilibrium interval defined as the imaging window where SUVR becomes stable over time was determined by visual inspection of the SUVR over time curves.

*Statistical Analysis.* Reproducibility of PET measurement (DVR and SUVR) was assessed by means of the test-retest variability (TRV) and intraclass correlation coefficient (ICC). TRV was calculated as the mean of the absolute differences of the test minus retest divided by the mean of test and retest expressed in percent ( $TRV = 200 \frac{|test - retest|}{(test + retest)}$ ). The ICC was calculated as  $\frac{[MSBS - MSWS]}{[MSBS + (k-1) MSWS]}$ , where MSBS and MSWS are the mean sum of squares between and within subjects, respectively, and k is the number of repeated observations (k=2 in this study). The effect size between AD subjects and HC was assessed by means of Cohen's d. DVR and SUVR measures were compared by means of linear regression.

## RESULTS

### Subject Demographics

A total of 9 HC and 4 AD subjects were assessed as part of these analyses. For the biodistribution and dosimetry study, 6 HC (3M/3F, 31.3±10.2 yrs) were included. Their demographics are shown in Supplemental Table 1. For the tracer kinetic study and test-retest scanning, three  $\beta$ -amyloid-negative HC (1M/2F, 67.0±7.2 yrs, MMSE range 29-30) and four  $\beta$ -amyloid-positive AD (3M/1F, 65.3±6.1 yrs, MMSE range: 15-28) were included. Subject demographics, clinical and  $\beta$ -amyloid PET status for these subjects are presented in Table 1 and more details are shown in the Supplemental Table 2. One AD subject's retest scan (#4) was non-evaluable due to substantial motion during acquisition and was excluded from the test-retest analysis. For the whole subject sample, no adverse events or serious adverse events related to the imaging agent  $^{18}\text{F}$ -PI-2620 were observed.

### Biodistribution and Dosimetry Study

$^{18}\text{F}$ -PI-2620 elimination was observed via both, the hepatobiliary and urinary system (Supplemental Figs. 1 and 2). The whole-body effective dose was determined to be 33.3±2.1  $\mu\text{Sv}/\text{MBq}$

(adult female) and  $33.1 \pm 1.4$   $\mu\text{Sv}/\text{MBq}$  (adult male) with a 1.5 hour urinary bladder voiding interval. The target organ with highest exposure (critical organ) was found to be the right colon in both adult female ( $222 \pm 28$   $\mu\text{Sv}/\text{MBq}$ ) and male ( $262 \pm 12$   $\mu\text{Sv}/\text{MBq}$ ) model. The individual organ residence times and doses are provided in Supplemental Tables 3, 4 and 5.

## Tracer Kinetics Study

*Visual Assessment.* No areas of specific  $^{18}\text{F}$ -PI-2620 retention were identified in HC subjects and a consistent pattern of initial uptake and fast wash-out was observed throughout (Fig. 1A). Asymmetrical tracer uptake was identified in cortical regions in three of the four AD subjects. (Fig. 1B). One AD subject (#4) showed only slightly increased tracer retention. Within each subject, the  $^{18}\text{F}$ -PI-2620 test and retest images were visually comparable (upper and lower row in Fig. 1A and B, respectively). Visual assessment of SUVR images at different imaging windows indicated similar pattern of tracer retention (Supplemental Fig. 3).

*Time-Activity Curves (TAC).* In the HC, both the cortex and cerebellar gray matter showed similar TAC patterns reaching peak around 5 min after injection and showing a rapid wash-out thereafter. In AD subjects, wash-out in areas of specific uptake was slower than in the HC, whereas the cerebellar cortex TACs were similar to those of the HC. Both HC and AD subjects displayed rapid clearance of the tracer in the reference region and across brain regions devoid of tau (Supplemental Fig. 4).

*Blood Sample Analyses.* Arterial blood measures were consistent between test and retest scans within each subject. No species more hydrophobic than the parent compound were detected indicating the probable absence of brain penetrating metabolites (Supplemental Fig. 5).  $^{18}\text{F}$ -PI-2620 metabolism was slightly faster in AD subjects compared with HC, where parent remaining at 30 min was  $12.7 \pm 5.0\%$  and  $19.6 \pm 5.1\%$  and at 90 min was  $7.7 \pm 4.0\%$  and  $11.0 \pm 3.8\%$ , respectively. Fifteen minutes after injection, the fraction of activity corresponding to unmetabolized parent compound in plasma dropped from the initial value to  $27 \pm 9.7\%$  (AD) and  $40.6 \pm 9.2\%$  (HC). Afterward, a slow decrease was observed until its final level ( $\sim 10\%$ ) was reached (Supplemental Fig. 5). Free fraction for test and retest scans, respectively, was  $0.52 \pm 0.24\%$  and  $0.43 \pm 0.31\%$  in AD subjects and  $0.38 \pm 0.11\%$  and  $0.33 \pm 0.02\%$  in HC subjects.

*Invasive Kinetic Models.* On visual inspection, the 2TC model including the cerebral cortical vascular fraction (vB) fitted the TACs adequately (Fig. 2). Poor fitting to the data was achieved using the 1TC (data not shown). The Akaike weights used as a model selection criterion favored the use of a 2TC model in all regions (AIC=  $-24.02 \pm 24.9$  (2TC),  $28.18 \pm 17.36$  (2TC, fixed vB=0.05),  $52.21 \pm 17.98$  (1TC, fixed

$vB=0.05$ ),  $79.68\pm 12.43$  (1TC)). The 2TC model provided lower AIC values in 99.31% of regions in comparison to the 2TC model with fixed  $vB$  ( $vB=0.05$ ) and 100% of the regions in comparison to 1TC with or without fixing  $vB$ . Therefore, 2TC model fitting with  $vB$  fitted (2TC- $vB$ ) was used for the successive analysis. Excellent agreement was found between DVR estimated with 2TC- $vB$  model and LGA ( $DVR(LGA)=0.20 + 0.81\cdot DVR(2TC-vB)$ ,  $R^2=0.98$ ) (Fig. 3).

*Non-invasive Kinetic Models.* Excellent correlation in DVR was found between 2TC- $vB$  model and non-invasive kinetic models. However, DVR from the NI-LGA and MRTM2 underestimated the DVR derived from the 2TC- $vB$  model ( $DVR(NI-LGA) = 0.31 + 0.69\cdot DVR(2TC-vB)$ ,  $R^2=0.97$ ;  $DVR(MRTM2) = 0.33 + 0.67\cdot DVR(2TC-vB)$ ,  $R^2=0.97$ ) (Fig. 3).

*SUVR.* Secular equilibrium was identified on visual inspection around 40 min p.i. in most regions and subjects. In some instances, secular equilibrium was not achieved and SUVR increased steadily during the whole scan (Fig. 4). Strong correlation was found between the  $DVR(2TC-vB)$  and SUVR for all imaging windows between 30 min p.i. and 90 min p.i. ( $R^2 > 0.95$ ) (Fig. 5).

*Test-Retest Variability, ICC and Effect Size.* Time elapsed between the two scans ranged from  $6\pm 3$  days (range 3-11 days). The lowest median test-retest variability across regions was achieved by means of tracer kinetic models (3.6%  $DVR(2TC-vB)$ , 3.6%  $DVR(LGA)$ , 2.8%  $DVR(NI-LGA)$ , 2.7% (MRTM2)) (Table 2). The minimum test-retest variability for SUVR was achieved at the imaging windows between 20 to 90 min (3.8% (30-60 min); 4.3% (45-75 min); 4.9% (60-90 min)). All methods analyzed showed excellent ICC values ( $>0.94$ ) (Table 2). Excellent discrimination between AD subjects and HC measured by means of the effect size was found (Cohen's  $d=2.75\pm 1.29$   $DVR(2TC-vB)$ ,  $3.30\pm 1.83$   $DVR(LGA)$ ,  $3.35\pm 1.84$   $DVR(NI-LGA)$ ,  $3.32\pm 1.80$  (MRTM2)). For the SUVR, the maximum effect size was achieved at imaging windows between 30 and 90 min ( $3.80\pm 2.11$  (30-60 min),  $3.77\pm 2.19$  (45-75 min),  $3.73\pm 2.27$  (60-90 min)) (Table 2).

*Shortened Scanning Time.* Analysis of SUVR for shortened imaging windows of 25 min (45-70 min p.i.), 20 min (50-70 min p.i.) and 10 min (55-65 min p.i.) showed only small differences with respect to the full 30-min acquisition. 90% of the cases were in the range of  $[-0.83, 0.84]\%$ ,  $[-1.06, 1.49]\%$  and  $[-1.80, 2.42]\%$ , respectively (Supplemental Fig. 6). Analysis of shortened scanning time also showed acceptable test-retest variability (median (90% quantile) = 4.3% (9.6%) (30 min), 4.0% (10.0%) (25 min), 4.3% (9.9%) (20 min) and 4.5% (11.0%) (10 min)).

## DISCUSSION

In this study, biodistribution and radiation dosimetry of  $^{18}\text{F}$ -PI-2620 were estimated from human whole-body PET data. The effective dose of  $^{18}\text{F}$ -PI-2620 is within the conventional range of  $^{18}\text{F}$  tracer radiation burden and allows longitudinal PET examinations in the same subject. Additionally,  $^{18}\text{F}$ -PI-2620 kinetic properties were characterized and the 2TC-vB model was identified as the optimal full kinetic modelling approach to quantify tau load in the human brain. The validity of non-invasive kinetic modeling and semi-quantitative methods were confirmed. The excellent reproducibility of  $^{18}\text{F}$ -PI-2620 PET measurements between test and retest scans further substantiate the promising initial clinical data and allow for further clinical investigations in larger studies.

Favorable  $^{18}\text{F}$ -PI-2620 tracer kinetics with fast wash-out from non-affected areas were observed and no signs of brain penetrating metabolites or defluorination. DVR estimated using non-invasive kinetic models (NI-LGA and MRTM2) showed excellent correlation to the invasive 2TC-vB model. This allows to apply a simple acquisition protocol for kinetic modelling without the need of arterial sampling thus reducing patient burden. Optimal performance of semi-quantitative quantification using SUVR was found in the 30 to 90 min imaging window with strong correlation to full tracer kinetic quantification and optimal test-retest variability, effect size and good visual discrimination between HC and AD subjects. Outside of the 30 to 90 min imaging window quantification accuracy, effect size, and test-retest variability were impaired. These results suggest that SUVR at the 30 to 90 min imaging window can be used for  $^{18}\text{F}$ -PI-2620 PET quantification of tau deposits with a simple protocol avoiding arterial blood sampling and dynamic scanning. Performance of different imaging window between 30 and 90 min p.i. was similar but scans at 45-75min p.i. provided a good compromise between early acquisition time after tracer injection, quantification accuracy, effect size, test-retest variability and visual assessment and can be recommended for static acquisitions. Further analysis of a shortened imaging window showed acceptable accuracy for a 20 min imaging window, which would be a good compromise for image accuracy and patient convenience. A relevant limitation of SUVR is that secular equilibrium was not reached during the whole acquisition in some regions. This potential drawback has also been described for other tau radiotracers (12-14). Although, the occasional lack of secular equilibrium will unlikely hinder visual assessment, it deserves further study specially in quantitative analysis of tau deposition especially for longitudinal assessment.

In all quantitative analyses, the cerebellar gray matter was used as reference region due to the lack of tau accumulation. However, given the non-specific uptake in the vermis of some subjects, this area and surrounding cerebellar cortex had to be removed from the reference region. In some papers, the

cerebellar cortex was eroded away from other regions to minimize contamination from other regions especially the inferior temporal and occipital cortex (12,13). This correction was not applied in this manuscript. A preliminary analysis showed that eroded cerebellar cortex did not provide appreciable quantitative changes but increased the test-retest variability possibly because erosion reduced the volume of the cerebellar cortex. The need of eroding or removing the superior layer of the cerebellar cortex may depend on the subjects included in the study, consequently the optimal reference region for  $^{18}\text{F}$ -PI-2620 deserves further analysis in an expanded sample.

## CONCLUSION

Kinetic and quantitative analyses demonstrate specific accumulation of  $^{18}\text{F}$ -PI-2620 in cerebral regions known to be affected by tau deposition in AD subjects. Whole-body analyses showed tracer elimination occurred via both the hepatobiliary and urinary system and suitable dosimetry was demonstrated.  $^{18}\text{F}$ -PI-2620 exhibits excellent kinetic properties and low TRV. DVR measured using the 2TC-vB model with arterial sampling correlated strongly with DVR measured by NI-LGA, MRTM2 and SUVR. SUVR can be used for  $^{18}\text{F}$ -PI-2620 PET quantification of tau deposits avoiding arterial blood sampling and dynamic scanning. Static  $^{18}\text{F}$ -PI-2620 PET scan acquisition in AD patients starting at 45 min p.i. provides an excellent quantification accuracy, large effect size and low TRV.

## **DISCLOSURES**

Andre Mueller, Santiago Bullich, Mathias Berndt, Norman Koglin, Caroline Papin, Susan de Santi, Ludger M. Dinkelborg and Andrew W. Stephens are employed by Life Molecular Imaging, who funded the clinical study. Audrey Perrotin serves as consultant for Life Molecular Imaging. Olivier Barret, Jennifer Madonia, Cristian Constantinescu, Christine Sandiego, Caroline Papin, Gilles Tamagnan, John P. Seibyl, Kenneth Marek were employed by MNI, Molecular Neuroimaging, LLC, now Invicro, who were contracted by Life Molecular Imaging to conduct the clinical study. Andrea Pfeifer and Heiko Kroth are employed by AC Immune and hold shares of AC Immune. No other potential conflict of interest relevant to this article was reported.

## **ACKNOWLEDGMENTS**

The authors thank all patients, their caregivers, and the healthy volunteers who participated in this trial. We are also grateful to the chemistry and clinical translational research staff at Invicro (formerly MNI) for their excellent technical assistance.

## **KEY POINTS**

**QUESTION:** Does  $^{18}\text{F}$ -PI-2620 show suitable pharmacokinetics and can non-invasive modeling approaches and SUVR-based quantification be applied to study tau depositions?

**PERTINENT FINDINGS:** This clinical study demonstrated suitable pharmacokinetics and dosimetry for  $^{18}\text{F}$ -PI-2620. SUVR-based quantification and non-invasive modeling approaches provide similar accuracy with low test-retest variability as compared to full tracer kinetics.

**IMPLICATIONS FOR PATIENT CARE:** Simplified imaging protocols and convenient time windows can be used for reliable  $^{18}\text{F}$ -PI-2620 PET quantification avoiding arterial blood sampling providing confidence for future longitudinal studies.

## REFERENCES

1. Villemagne VL, Dore V, Burnham SC, Masters CL, Rowe CC. Imaging tau and amyloid-beta proteinopathies in Alzheimer disease and other conditions. *Nat Rev Neurol*. 2018;14:225-236.
2. Leuzy A, Chiotis K, Lemoine L, et al. Tau PET imaging in neurodegenerative tauopathies—still a challenge. *Mol Psychiatry*. 2019;24:1112-1134.
3. Schöll M, Maass A, Mattsson N, et al. Biomarkers for tau pathology. *Mol Cell Neurosci*. 2019;97:18-33.
4. Kroth H, Oden F, Molette J, et al. Discovery and preclinical characterization of [(18)F]PI-2620, a next-generation tau PET tracer for the assessment of tau pathology in Alzheimer's disease and other tauopathies. *Eur J Nucl Med Mol Imaging*. 2019;46:2178-2189.
5. Mueller A, Bullich S, Barret O, et al. Tau PET imaging with 18F-PI-2620 in patients with Alzheimer's disease and healthy controls: a first-in-human study. *J Nucl Med*. 2019;60:153-161.
6. Stabin MG, Sparks RB, Crowe E. OLINDA/EXM: the second-generation personal computer software for internal dose assessment in nuclear medicine. *J Nucl Med*. 2005;46:1023-1027.
7. Sanabria Bohorquez S, Marik J, Ogasawara A, et al. [(18)F]GTP1 (Genentech Tau Probe 1), a radioligand for detecting neurofibrillary tangle tau pathology in Alzheimer's disease. *Eur J Nucl Med Mol Imaging*. 2019; 46:2077-2089.
8. Tzourio-Mazoyer N, Landeau B, Papathanassiou D, et al. Automated anatomical labeling of activations in SPM using a macroscopic anatomical parcellation of the MNI MRI single-subject brain. *Neuroimage*. 2002;15:273-289.
9. Innis RB, Cunningham VJ, Delforge J, et al. Consensus nomenclature for in vivo imaging of reversibly binding radioligands. *J Cereb Blood Flow Metab*. 2007;27:1533-1539.
10. Logan J. Graphical analysis of PET data applied to reversible and irreversible tracers. *Nucl Med Biol*. 2000;27:661-670.
11. Ichise M, Liow JS, Lu JQ, et al. Linearized reference tissue parametric imaging methods: application to [11C]DASB positron emission tomography studies of the serotonin transporter in human brain. *J Cereb Blood Flow Metab*. 2003;23:1096-1112.
12. Barret O, Alagille D, Sanabria S, et al. Kinetic modeling of the Tau PET tracer (18)F-AV-1451 in human healthy volunteers and Alzheimer disease subjects. *J Nucl Med*. 2017;58:1124-1131.

- 13.** Kuwabara H, Comley RA, Borroni E, et al. Evaluation of (18)F-RO-948 PET for quantitative assessment of tau accumulation in the human brain. *J Nucl Med.* 2018;59:1877-1884.
  
- 14.** Guehl NJ, Wooten DW, Yokell DL, et al. Evaluation of pharmacokinetic modeling strategies for in-vivo quantification of tau with the radiotracer [(18)F]MK6240 in human subjects. *Eur J Nucl Med Mol Imaging.* 2019;46:2099-2111.

## FIGURES

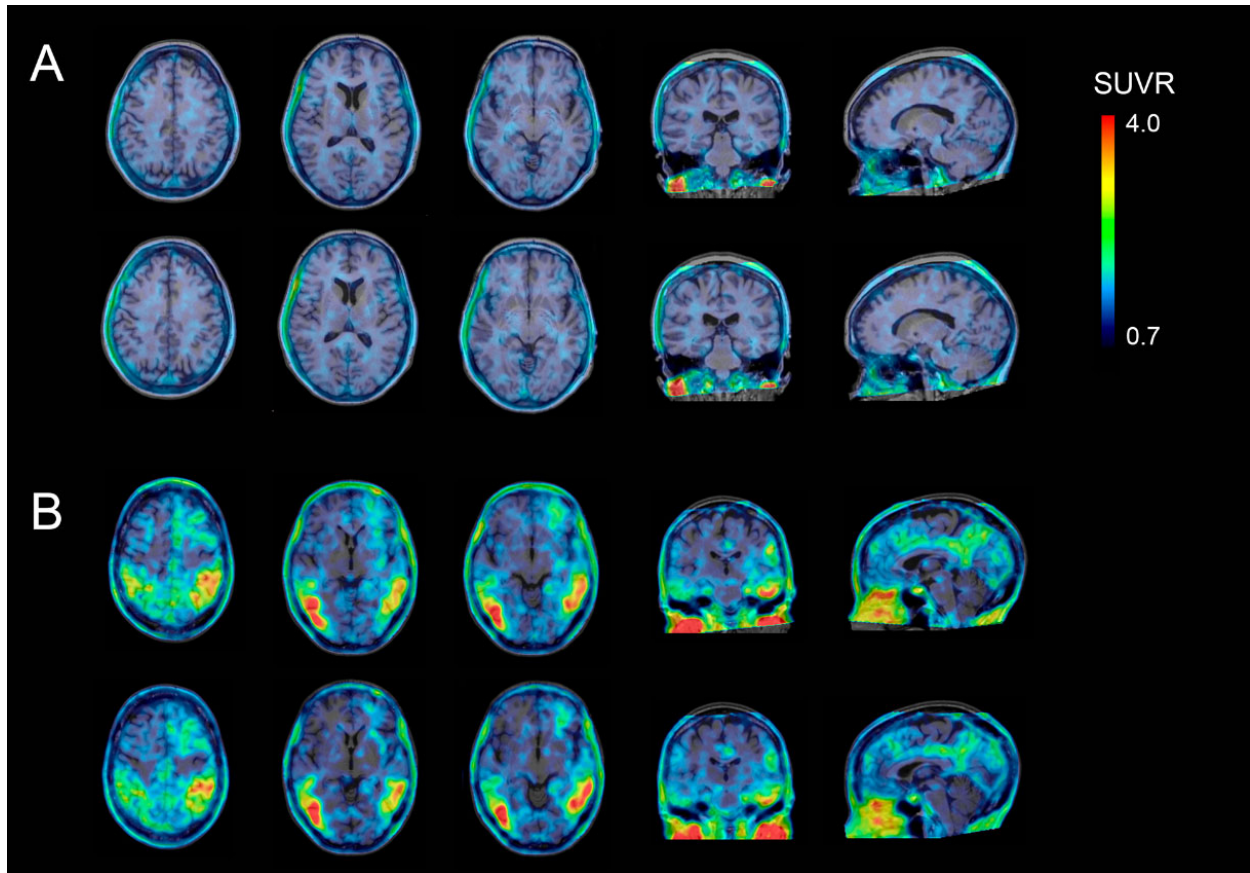


**FIGURE 1.**  $^{18}\text{F}$ -PI-2620 test and retest SUVR images (45-75 min) (A) Images from a HC are shown (subject #01; 65 years old, MMSE=29, CDR 0, ADAS-Cog=5). (B) Images from an AD subject are shown (subject #06; 62 years old, MMSE=28, CDR 0.5, ADAS-Cog=16). The upper row in each panel shows the test images and the lower row the retest images. Scans were normalized to the cerebellar gray matter and were co-registered to the MRI.

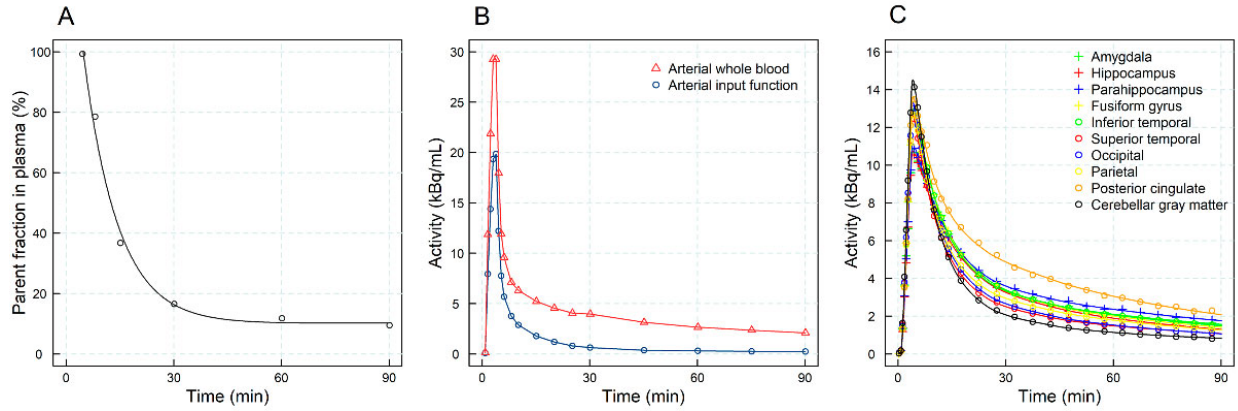


**FIGURE 2.** (A) Percent parent fraction in arterial plasma after intravenous injection of  $^{18}\text{F}$ -PI-2620 including a biexponential function fit of a representative AD subject (#5). (B) Metabolite corrected arterial plasma concentration and arterial whole blood concentration of  $^{18}\text{F}$ -PI-2620 from the same case shown in A. (C) Time-activity curves from selected brain regions with the 2TC-vB model fitting of the same case shown in A.

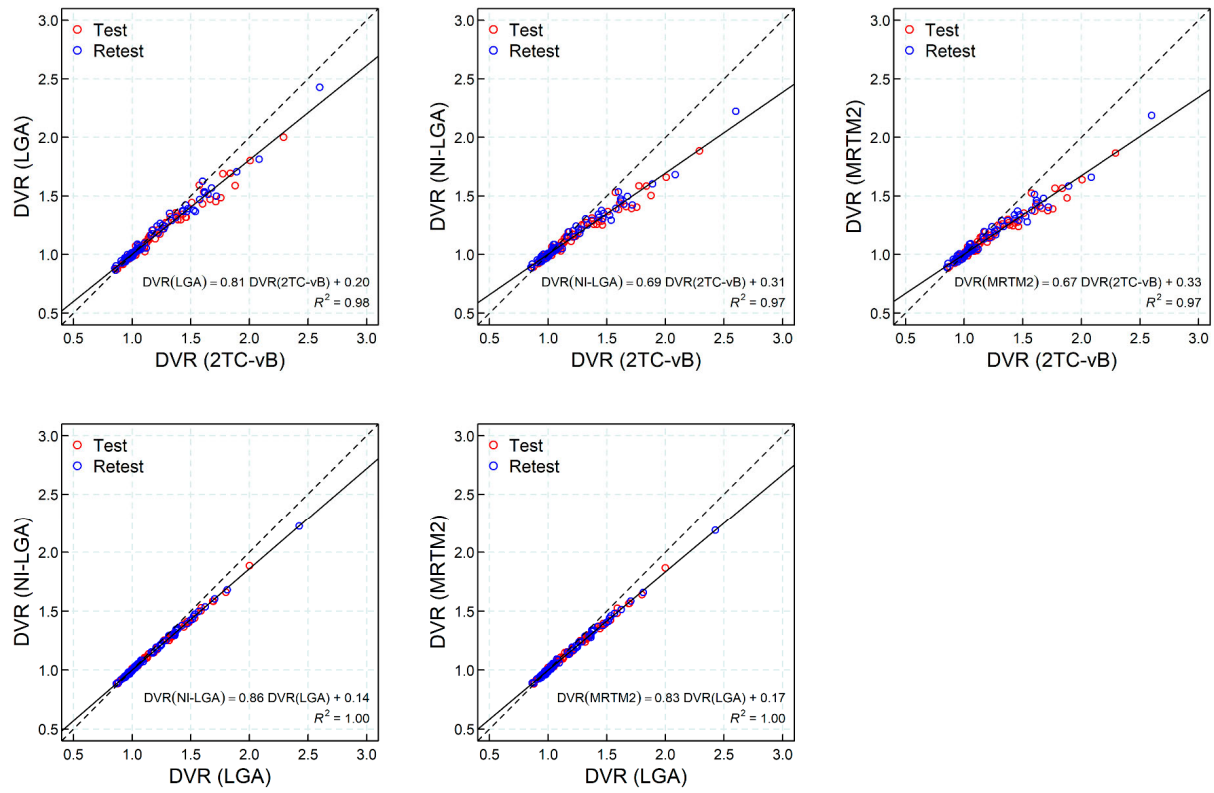


**FIGURE 3.** Regression analysis between DVR obtained using invasive models (2TC-vB and LGA) and non-invasive kinetic models (NI-LGA and MRTM2). Solid line corresponds to the linear regression fitting and dashed line corresponds to the identity line.

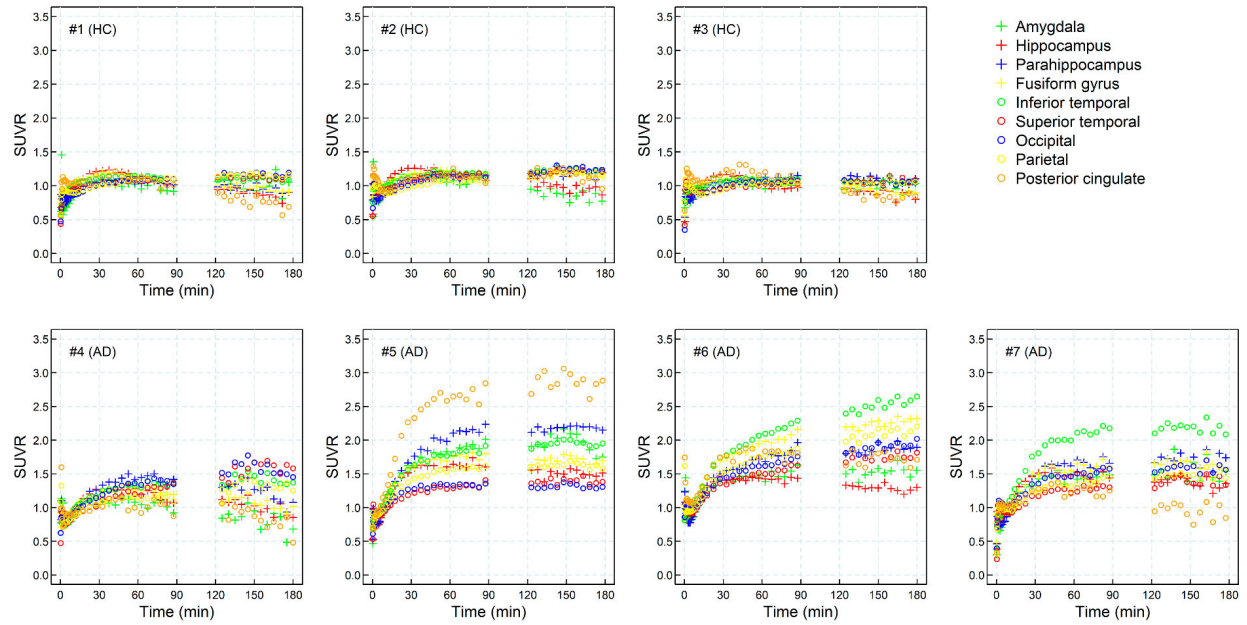


**FIGURE 4.** SUVR time curves of all ‘test’  $^{18}\text{F}$ -PI-2620 PET scans included in the study (average of left and right hemispheres).

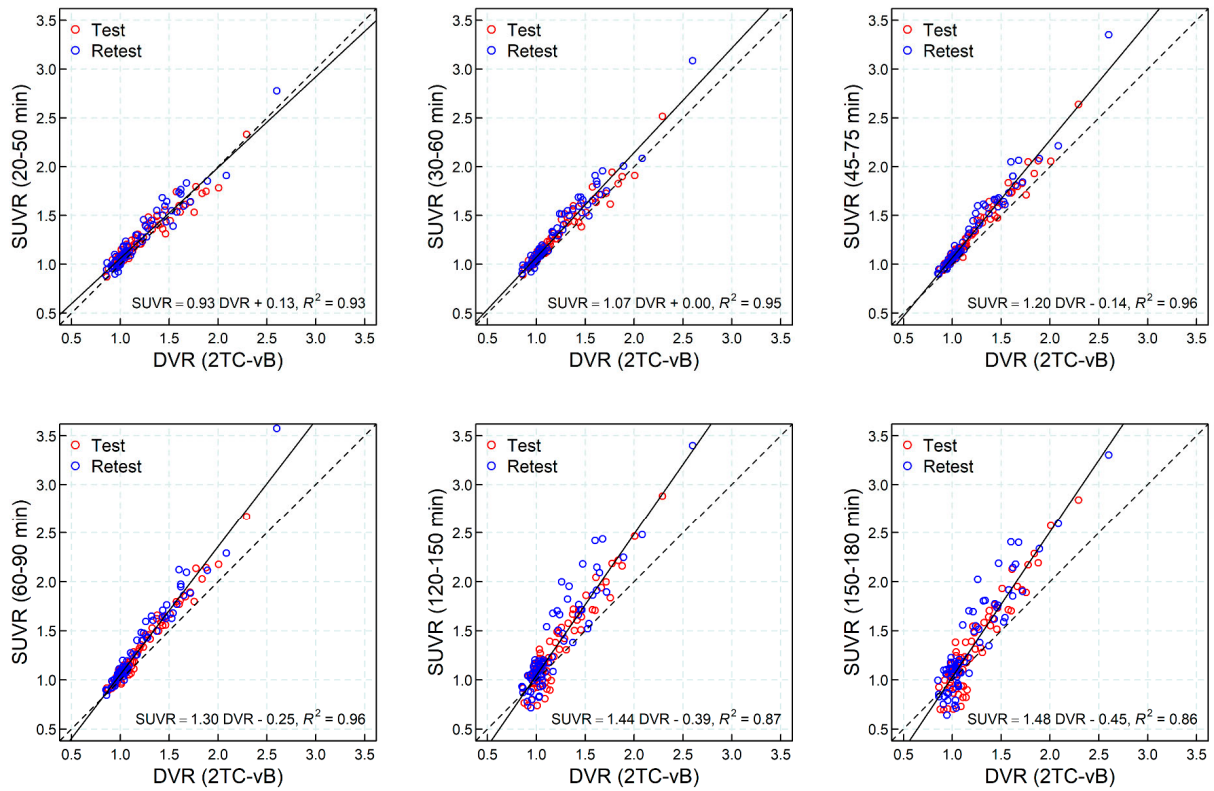


**FIGURE 5.** Regression analysis between DVR obtained using invasive 2TC-vB and SUVR at different imaging windows: 20-50 min, 30-60 min, 45-75 min, 60-90 min, 120-150 min and 150-180 min. Solid line corresponds to the linear regression fitting and dashed line corresponds to the identity line.

## TABLES

**TABLE 1.** Demographics for subjects enrolled in the tracer kinetics study.

Subject ID	Gender	Age (yrs)	Cohort	$\beta$ -amyloid visual interpretation	ADAS-Cog Score	CDR Score	MMSE Score
1	Female	65	HC	Negative	5	0	29
2	Female	75	HC	Negative	7	0	30
3	Male	61	HC	Negative	3	0	30
4*	Male	70	AD	Positive	30	1	15
5	Male	58	AD	Positive	19	0.5	20
6	Female	62	AD	Positive	16	0.5	28
7	Male	71	AD	Positive	22	0.5	20

\* Subject number #4 did not complete the two imaging sessions.

**TABLE 2.** Absolute value of the percent test-retest variability (TRV), intraclass correlation coefficient (ICC) and Cohen’s d across all regions analyzed.

	<b>TRV*</b>	<b>ICC†</b>	<b>d‡</b>
DVR (2TC-vB)	3.6 (10.2)	0.96 (0.94)	2.75±1.29
DVR (LGA)	3.6 (10.2)	0.96 (0.93)	3.30±1.83
DVR (NI-LGA)	2.8 (6.2)	0.96 (0.92)	3.35±1.84
DVR (MRTM2)	2.7 (5.9)	0.96 (0.92)	3.32±1.80
SUVR (20-50 min)	4.2 (8.7)	0.94 (0.92)	3.65±2.10
SUVR (30-60 min)	3.8 (9.5)	0.95 (0.92)	3.80±2.11
SUVR (45-75 min)	4.3 (9.6)	0.96 (0.92)	3.77±2.19
SUVR (60-90 min)	4.9 (9.6)	0.96 (0.90)	3.73±2.27
SUVR (120-150 min)	5.4 (13.2)	0.96 (0.91)	3.36±1.90
SUVR (150-180 min)	5.7 (14.9)	0.96 (0.93)	3.28±1.82

\* Median and 90% quantile (i.e. 90% of the cases have a TRV below this value)

† Median and 10% quantile (i.e. 10% of the cases have an ICC below this value)

‡ Mean ± SD

## SUPPLEMENTAL DATA

**Supplemental Table 1.** Demographics for the subjects enrolled in the biodistribution and dosimetry study.

Subject ID	Gender	Age (yrs)	Race	Weight (kg)	Dose (MBq)	Tracer mass dose ( $\mu\text{g}$ )
08	Male	39	Black or African American	73.0	345.4	1.47
09	Female	28	Black or African American	99.8	354.8	0.8
10	Female	24	Black or African American	64.4	358.1	1.26
11	Male	31	Hispanic	96.2	354.9	1.10
12	Male	47	White	88.5	350.2	0.74
13	Female	19	White	73.0	358.0	1.06
Mean $\pm$ SD		31.3 $\pm$ 10.2		82.5 $\pm$ 14.6	353.6 $\pm$ 4.9	1.1 $\pm$ 0.3

**Supplemental Table 2.** Demographics for the subjects enrolled in the tracer kinetics study.

Subject ID	Gender	Age (yrs)	Race	Weight (kg)	Dose (MBq) Test	Tracer mass dose ( $\mu$ g) Test	Dose (MBq) Retest	Tracer mass dose ( $\mu$ g) Retest
1	Female	65	White	68.5	341.3	2.5	336.3	3.3
2	Female	75	Black/Indian	62.6	339.7	2.4	323.3	1.4
3	Male	61	White	80.3	333.3	1.2	341.7	0.9
4*	Male	70	Hispanic	68.5	346.7	1.0	340.4	1.6
5	Male	58	Hispanic	86.6	346.1	0.8	344.2	2.4
6	Female	62	White	62.6	333.4	1.0	348.2	6.5
7	Male	71	White	108.8	335.3	1.1	343.9	1.3
Mean $\pm$ SD		66 $\pm$ 5.7		76.8 $\pm$ 15.5	339.4 $\pm$ 5.2	1.4 $\pm$ 0.7	339.7 $\pm$ 7.5	2.1 $\pm$ 1.1

\* Subject number #4 did not complete the two imaging sessions.

**Supplemental Table 3.** Individual residence times (i.e. number of disintegrations) in source organs expressed in MBq·h/MBq. The urinary bladder values without voiding modeling and with a 1.5-hour voiding interval (\*) are given.

Target organ	Subject ID					
	08 (#2)	09 (#3)	10 (#4)	11 (#5)	12 (#6)	13 (#7)
Brain	1.83E-02	2.09E-02	2.58E-02	1.46E-02	1.71E-02	2.21E-02
Gallbladder Cont.	3.45E-02	2.18E-02	9.16E-02	7.13E-02	4.88E-02	7.52E-03
Lower large intestine	7.37E-02	5.49E-02	6.58E-02	7.90E-02	7.28E-02	7.17E-02
Small intestine	7.35E-01	5.47E-01	6.55E-01	7.87E-01	7.25E-01	7.14E-01
Stomach	9.92E-03	9.33E-03	1.79E-02	1.25E-02	3.34E-02	2.38E-02
Upper large intestine	4.03E-01	3.00E-01	3.59E-01	4.32E-01	3.98E-01	3.92E-01
Heart Wall	9.66E-03	1.28E-02	6.86E-03	8.80E-03	1.29E-02	1.20E-02
Kidneys	4.19E-02	6.86E-02	7.10E-02	3.25E-02	4.44E-02	3.72E-02
Liver	3.48E-01	3.71E-01	3.03E-01	4.03E-01	3.72E-01	3.69E-01
Lungs	4.38E-02	2.92E-02	3.41E-02	2.72E-02	7.41E-02	2.79E-02
Red Marrow †	3.21E-02	3.86E-02	5.71E-02	2.84E-02	2.44E-02	2.50E-02
Spleen	6.91E-03	1.03E-02	4.44E-03	4.21E-03	6.85E-03	5.14E-03
Urinary Bladder Content	1.05E-01	2.15E-01	2.22E-01	1.19E-01	1.47E-01	1.64E-01
Urinary Bladder Content (*)	9.22E-02	1.98E-01	1.77E-01	1.31E-01	1.57E-01	1.49E-01
Remainder	7.78E-01	9.40E-01	7.25E-01	6.19E-01	6.64E-01	7.69E-01

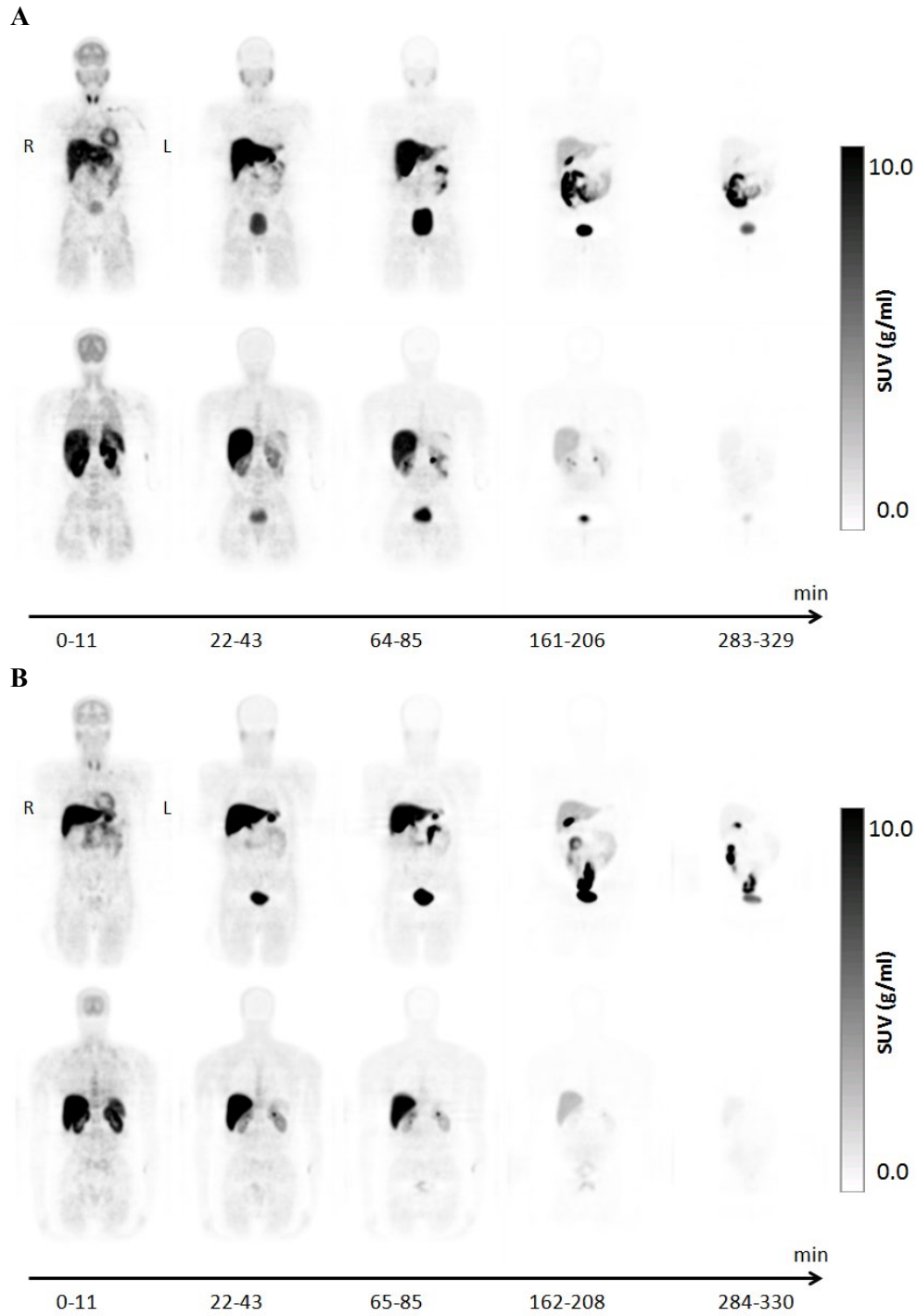
† To estimate the whole-body marrow content the residence time measure in lumbar spine was divided by 0.4 (40%), based on information provided in literature on the values of red marrow mass (see Cristy M. Active bone marrow distribution as a function of age in humans. Phys.Med.Biol. 1981 May;26(3):389-400).

**Supplemental Table 4.** <sup>18</sup>F-PI-2620 target organ and radiation exposure summary (radiation doses expressed in mSv/MBq) using ICRP-89 adult female and male phantoms and ICRP-103 tissue weighting factors with no modelling of urinary bladder voiding. The organ with the largest absorbed dose is shown in bold font.

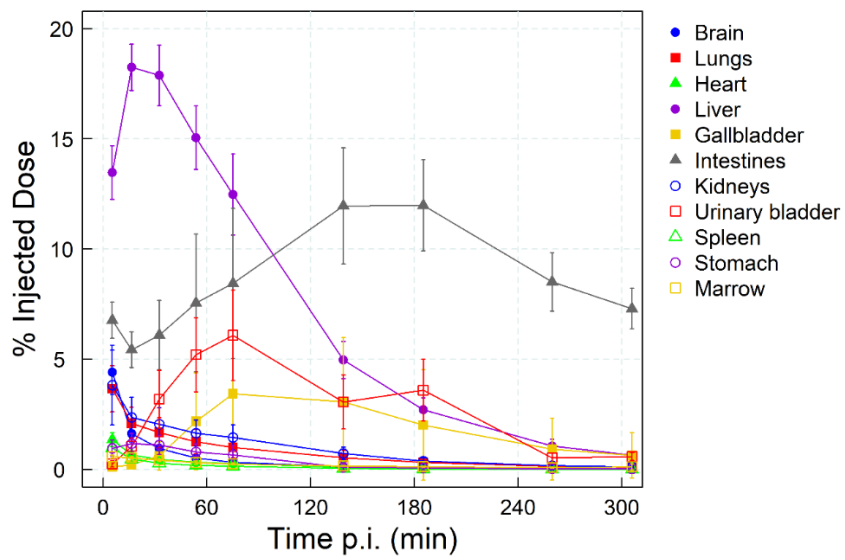
Target Organ	Female			Male		
	[mSv/MBq]			[mSv/MBq]		
	mean ± SD			mean ± SD		
Adrenals	2.43E-02	±	1.03E-03	2.56E-02	±	5.13E-04
Brain	5.51E-03	±	3.87E-04	3.64E-03	±	3.92E-04
Breasts	6.34E-03	±	5.12E-04	--		--
Esophagus	1.12E-02	±	6.51E-04	1.02E-02	±	4.88E-04
Eyes	1.53E-02	±	2.50E-03	1.13E-02	±	3.59E-03
Gallbladder Wall	1.13E-01	±	8.67E-02	1.23E-01	±	3.24E-02
Left colon	7.30E-02	±	7.57E-03	1.04E-01	±	4.36E-03
Small Intestine	2.17E-01	±	2.65E-02	2.09E-01	±	8.72E-03
Stomach Wall	2.35E-02	±	3.40E-03	1.96E-02	±	5.34E-03
<b>Right colon</b>	<b>2.25E-01</b>	±	<b>2.80E-02</b>	<b>2.63E-01</b>	±	<b>1.19E-02</b>
Rectum	2.99E-02	±	1.04E-03	3.13E-02	±	6.35E-04
Heart Wall	1.49E-02	±	2.40E-03	1.54E-02	±	1.50E-03
Kidneys	5.62E-02	±	1.22E-02	3.82E-02	±	3.22E-03
Liver	6.65E-02	±	5.20E-03	5.92E-02	±	4.16E-03
Lungs	1.24E-02	±	3.46E-04	1.33E-02	±	3.37E-03
Ovaries	2.21E-02	±	4.16E-04	--		--
Pancreas	3.02E-02	±	1.21E-03	3.05E-02	±	7.64E-04
Prostate	--		--	1.47E-02	±	3.79E-04
Salivary Glands	5.18E-03	±	5.76E-04	3.89E-03	±	4.16E-04
Red Marrow	1.45E-02	±	1.40E-03	1.01E-02	±	3.44E-04
Osteogenic Cells	9.38E-03	±	6.92E-04	7.30E-03	±	3.12E-04
Spleen	2.18E-02	±	3.96E-03	1.63E-02	±	2.03E-03
Testes	--		--	4.94E-03	±	3.13E-04
Thymus	7.96E-03	±	6.68E-04	6.59E-03	±	4.48E-04
Thyroid	5.94E-03	±	6.04E-04	4.86E-03	±	4.56E-04
Urinary Bladder Wall	1.23E-01	±	1.74E-02	6.86E-02	±	1.01E-02
Uterus	3.04E-02	±	1.03E-03	--		--
Total Body	1.59E-02	±	5.77E-05	1.10E-02	±	5.77E-05
<b>Effective dose (ED, ICRP-103)</b>	<b>3.59E-02</b>	±	<b>2.05E-03</b>	<b>3.41E-02</b>	±	<b>1.43E-03</b>

**Supplemental Table 5.**  $^{18}\text{F}$ -PI-2620 target organ and radiation exposure summary (radiation doses expressed in mSv/MBq) using ICRP-89 adult female and male phantoms and ICRP-103 tissue weighting factors with a 1.5 hour urinary bladder voiding interval. The organ with the largest absorbed dose is shown in bold font.

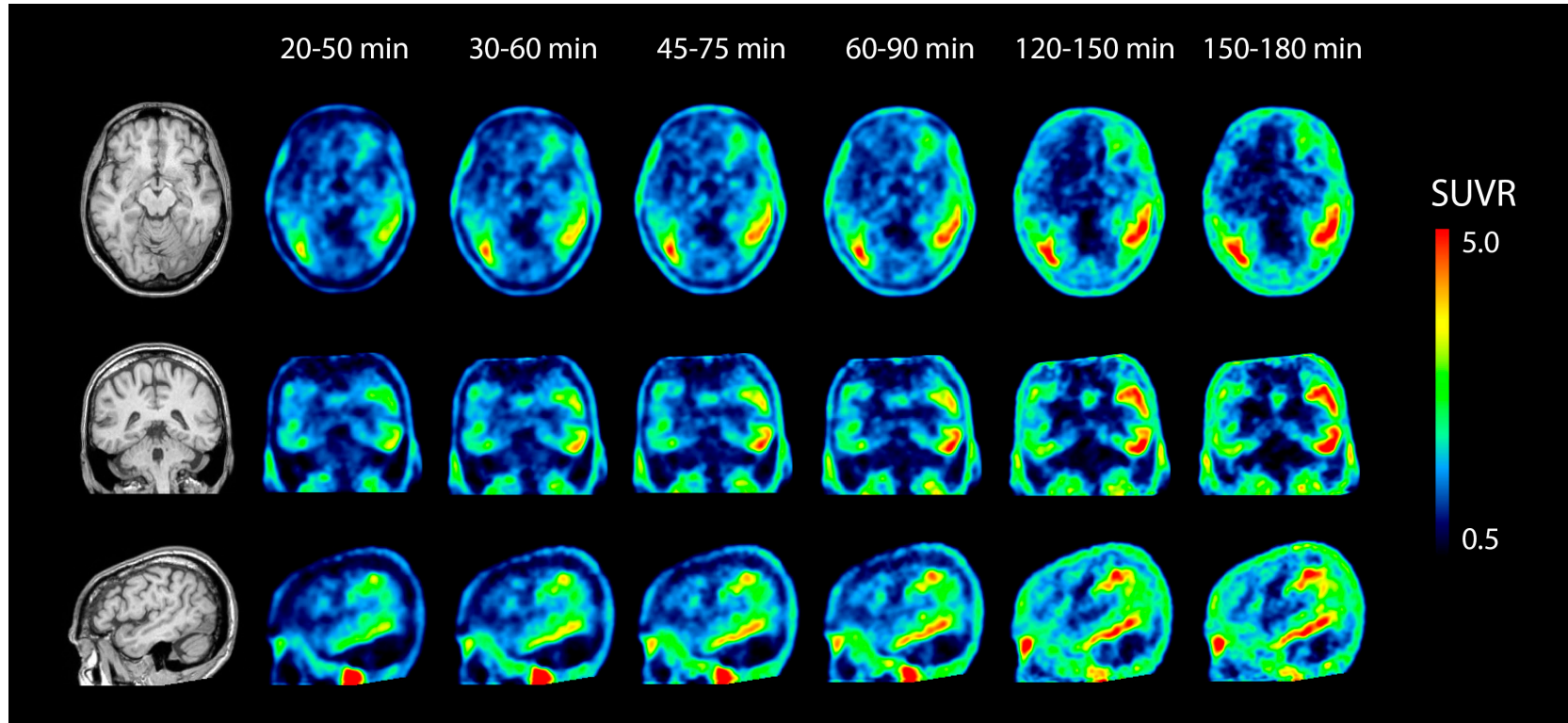
<b>Target Organ</b>	<b>Female</b> <b>[mSv/MBq]</b> <b>mean <math>\pm</math> SD</b>			<b>Male</b> <b>[mSv/MBq]</b> <b>mean <math>\pm</math> SD</b>		
Adrenals	2.19E-02	$\pm$	7.23E-04	2.41E-02	$\pm$	2.89E-04
Brain	4.88E-03	$\pm$	4.34E-04	3.26E-03	$\pm$	4.57E-04
Breasts	4.25E-03	$\pm$	2.26E-04	--		--
Esophagus	9.13E-03	$\pm$	4.33E-04	8.67E-03	$\pm$	4.26E-04
Eyes	1.43E-02	$\pm$	2.50E-03	1.06E-02	$\pm$	3.80E-03
Gallbladder Wall	1.11E-01	$\pm$	8.69E-02	1.22E-01	$\pm$	3.20E-02
Left colon	7.01E-02	$\pm$	7.99E-03	1.02E-01	$\pm$	4.16E-03
Small Intestine	2.14E-01	$\pm$	2.75E-02	2.07E-01	$\pm$	8.89E-03
Stomach Wall	2.10E-02	$\pm$	3.76E-03	1.80E-02	$\pm$	5.03E-03
<b>Right colon</b>	<b>2.22E-01</b>	$\pm$	<b>2.80E-02</b>	<b>2.62E-01</b>	$\pm$	<b>1.17E-02</b>
Rectum	2.57E-02	$\pm$	4.04E-04	2.95E-02	$\pm$	7.64E-04
Heart wall	1.34E-02	$\pm$	2.29E-03	1.45E-02	$\pm$	1.32E-03
Kidneys	5.49E-02	$\pm$	1.21E-02	3.74E-02	$\pm$	3.21E-03
Liver	6.54E-02	$\pm$	5.14E-03	5.86E-02	$\pm$	4.06E-03
Lungs	1.11E-02	$\pm$	2.65E-04	1.25E-02	$\pm$	3.23E-03
Ovaries	1.86E-02	$\pm$	7.00E-04	--		--
Pancreas	2.74E-02	$\pm$	1.70E-03	2.88E-02	$\pm$	4.93E-04
Prostate	--		--	1.29E-02	$\pm$	2.08E-04
Salivary Glands	2.86E-03	$\pm$	1.96E-04	2.27E-03	$\pm$	8.05E-04
Red Marrow	1.22E-02	$\pm$	1.37E-03	8.68E-03	$\pm$	6.45E-04
Osteogenic Cells	7.32E-03	$\pm$	6.03E-04	5.96E-03	$\pm$	6.41E-04
Spleen	2.05E-02	$\pm$	3.73E-03	1.55E-02	$\pm$	2.05E-03
Testes	--		--	2.05E-03	$\pm$	5.73E-04
Thymus	5.47E-03	$\pm$	3.12E-04	5.03E-03	$\pm$	6.20E-04
Thyroid	3.58E-03	$\pm$	2.30E-04	3.22E-03	$\pm$	7.39E-04
Urinary Bladder Wall	1.07E-01	$\pm$	1.32E-02	6.83E-02	$\pm$	1.51E-02
Uterus	2.61E-02	$\pm$	3.51E-04	--		--
Total Body	1.33E-02	$\pm$	4.73E-04	9.43E-03	$\pm$	4.47E-04
<b>Effective dose (ED, ICRP-103)</b>	<b>3.33E-02</b>	$\pm$	<b>2.08E-03</b>	<b>3.31E-02</b>	$\pm$	<b>1.40E-03</b>



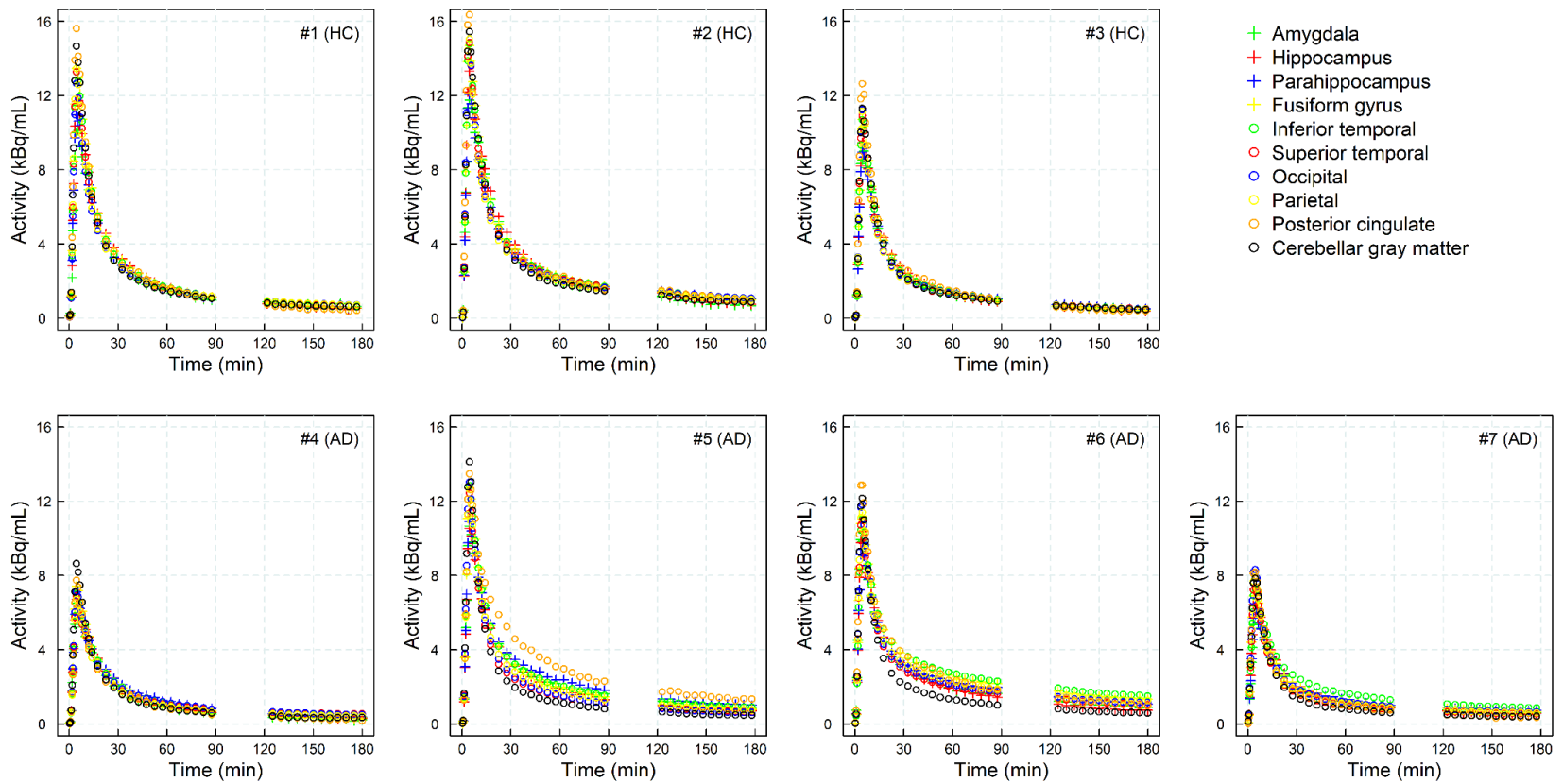
**Supplemental Figure 1.**  $^{18}\text{F}$ -PI-2620 whole body coronal sections showing the tracer distribution change over time in a healthy female (#09) subject (**A**) and in a healthy male (#11) subject (**B**). The two rows represent two different coronal slices at 5 time points. Images were smoothed prior to display using a 12 mm Gaussian filter.



**Supplemental Figure 2.** Non-decay corrected time-activity curves of  $^{18}\text{F}$ -PI-2620 in several organs (total activity) following a bolus injection. Total radioactivity in urine for all subjects measured over up to 6 hours post injection of  $^{18}\text{F}$ -PI-2620 was on average  $35.7 \pm 8\% \text{ID}$  (range:  $23.2 - 48.2\% \text{ID}$ ).

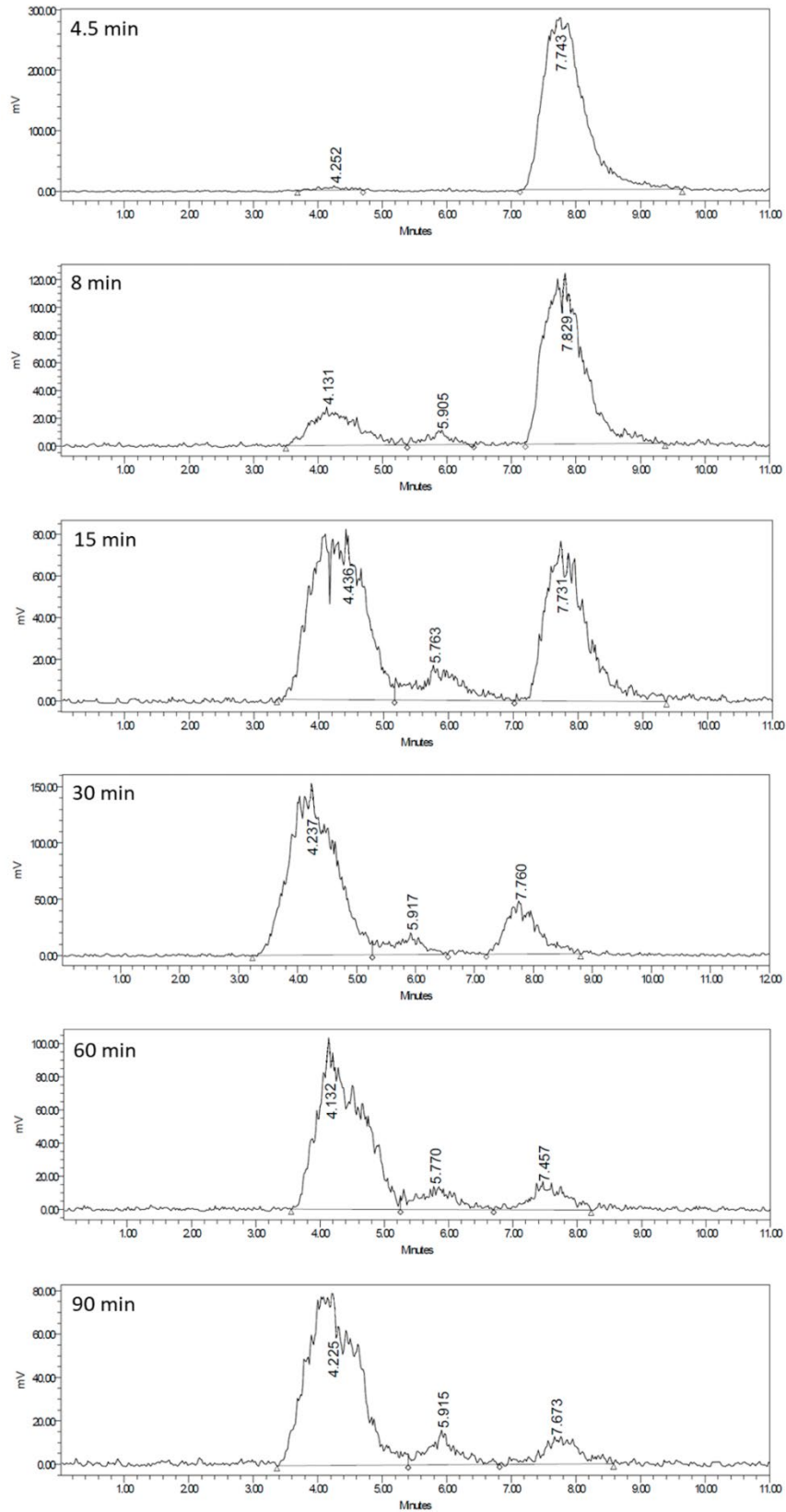


**Supplemental Figure 3.** Illustrative  $^{18}\text{F}$ -PI-2620 scans of an AD subject over different time windows.

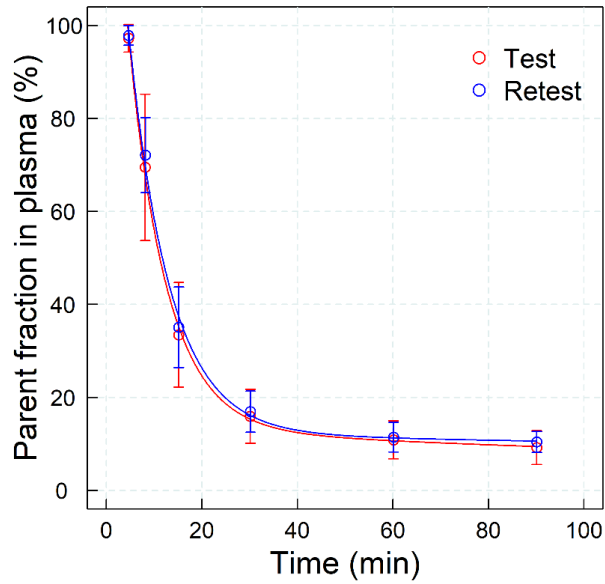


**Supplemental Figure 4.** Time-activity curves of all ‘test’  $^{18}\text{F}$ -PI-2620 PET scans included in the study (average of left and right hemispheres).

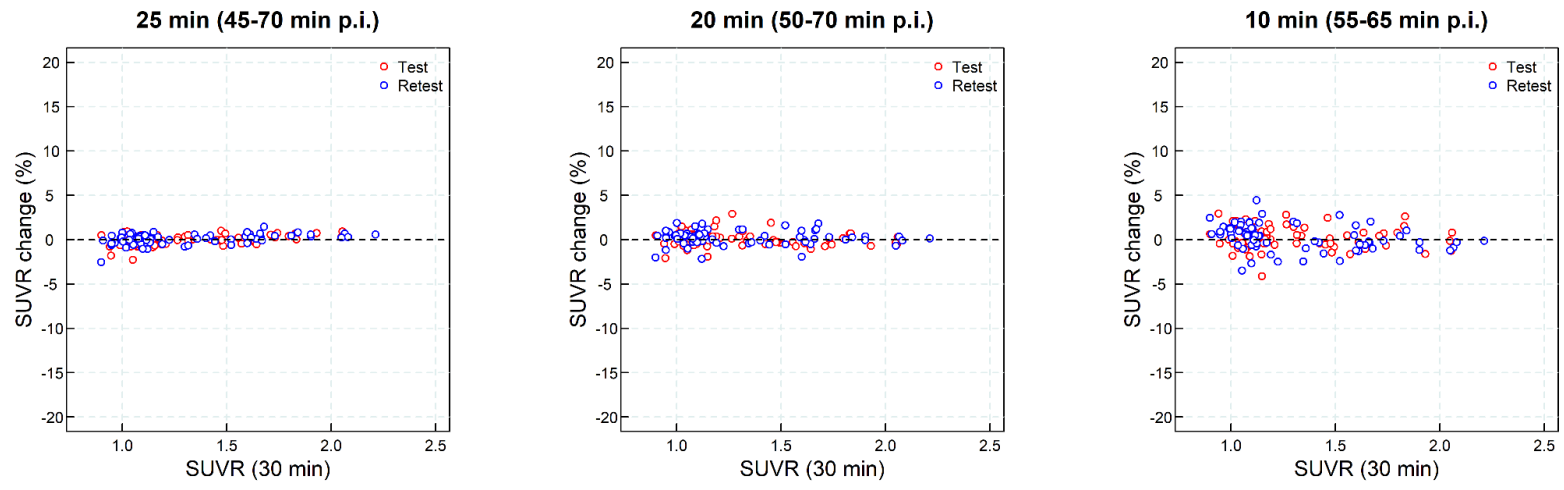
A



B



**Supplemental Figure 5. (A)** Illustrative chromatograms obtained from arterial blood samples drawn at indicated times after injection. **(B)** Average ( $\pm$ SD) of the parent compound in arterial plasma in test and retest including a biexponential function fit ( $p = \alpha e^{-\frac{t-t_0}{\tau_1}} + (100 - \alpha)e^{-\frac{t-t_0}{\tau_2}}$ ) with the following parameters ( $\alpha=86.8$ ,  $\tau_1=7.94$  min,  $\tau_2=256.3$  min,  $t_0 = 4.44$  min (test) and  $\alpha=87.7$ ,  $\tau_1=8.55$  min,  $\tau_2=574.2$  min,  $t_0 = 4.53$  min (retest))



**Supplemental Figure 6.** Changes in SUVR after shortening of the 30 min imaging window.